

Kinetic Modeling of the SWNT Growth by CO Disproportionation on CoMo Catalysts

A. Monzon[†], G. Lolli, S. Cosma, S. B. Mohamed, and D. E. Resasco*

School of Chemical Biological and Materials Engineering, University of Oklahoma, Norman, Oklahoma 73019, USA

A kinetic model has been developed to describe the growth of single-walled carbon nanotubes (SWNT) in the CoMoCAT™ method, which is based on the disproportionation of CO on supported CoMo catalysts. The model attempts to capture mathematically the different stages involved in this method: (i) *catalyst activation* or *in-situ* creation of active sites, i.e., reduced Co clusters by transformation of CoMoO_x precursor species, or oxidized sites; (ii) *CO decomposition* over active sites, which increases the surface fugacity of carbon until reaching a certain threshold; (iii) *nucleation* of ordered forms of carbon; (iv) *C diffusion* (both across the surface and into the metal particle); (v) SWNT growth; (vi) *termination*, by either deactivation of the catalyst active sites or by increase in the carbon concentration at the metal/SWNT interface, approaching that of the metal/gas interface and eliminating the driving force for diffusion. Previous investigations have only explained the growth termination by the former. Here, we emphasize the possible contribution of the later and propose a novel “hindrance factor” to quantify the effect of nanotube interaction with its surroundings on the growth termination. To test the kinetic model and obtain typical values of the physical parameters, experiments have been conducted on a CoMo/SiO₂ catalyst in a laboratory flow reactor, in which the rate of carbon deposition was continuously evaluated by the direct measurement of the CO₂ evolution as a function of time. The experimental data are fitted very well with model.

Keywords: SWNT Growth, CoMoCAT Process, Kinetic Modeling, Co-Mo Catalysts.

1. INTRODUCTION

In the past few years, our group has investigated the disproportionation of CO on supported CoMo catalysts^{1–9} and has given ample evidence that this reaction can produce single-walled carbon nanotubes (SWNT) with high selectivity to the wanted product as opposed to other less desired forms of carbon, such as graphite nanofibers. In fact, the commercial CoMoCAT™ process, based on this reaction, currently makes SWNT with narrow diameter and chirality distributions.^{10–18} The advantage of modeling a selective process like this is that one does not need to take into account the different rates and kinetic parameters that would be required if different forms of carbon were produced.

As discussed in previous publications^{1–9} and illustrated in Figure 1, the CoMoCAT process involves a series of phase transformations of the CoMo species before starting the growth of SWNT. Prior to the incorporation of CO in the feed, the catalyst is first calcined in air and then

pre-reduced in hydrogen. After this calcination/reduction pre-treatment, the Co-Mo dual oxide species (mostly CoMoO₄) generated during the calcination step, ends up as a partially reduced bimetallic suboxide (CoMoO_x). This partially reduced suboxide has a significant number of oxygen vacancies which make the suboxide very reactive towards CO. When CO is admitted in the reactor at the reaction temperature, the CoMoO_x is carburized and decomposes into molybdenum carbide and metallic Co clusters that are the active species for the nanotube growth.^{5–9} Subsequently, further carbon deposition leads to the nucleation of the characteristic hemispherical caps that template the growth of SWNT.^{19–22} In this growth process, diffusion of carbon atoms through and/or over the metal particles, plays an important role as demonstrated by recent molecular dynamics simulations for small catalytic particles.^{23–25} The termination of the SWNT growth can be due to either catalyst deactivation or steric hindrance effects that will be discussed in this paper. In summary, the overall nanotube synthesis process can be described by the sequence:

- (a) catalyst carburization and activation
- (b) CO dissociation on the catalyst surface

* Author to whom correspondence should be addressed.

[†] Present address: On leave from Department of Chemical and Environmental Engineering, University of Zaragoza, Spain.

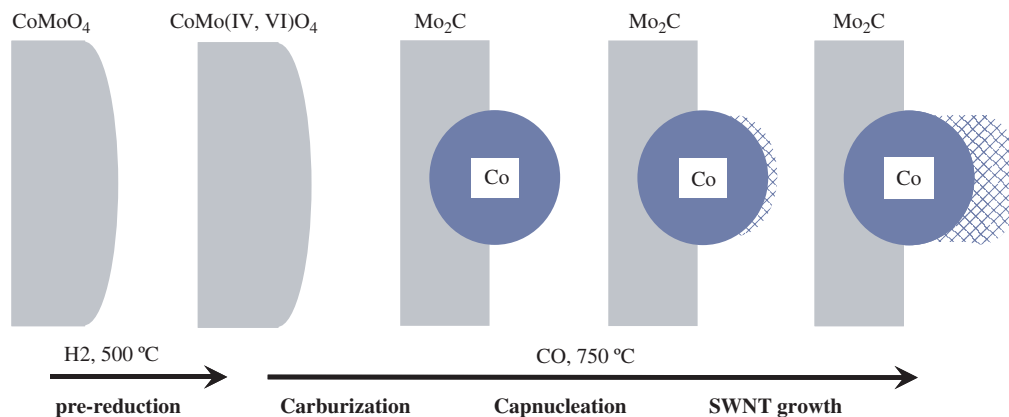


Fig. 1. Phase transformations leading to the formation of SWNT on Co-Mo/Silica catalysts during the various stages after calcination (pre-reduction, carburization, nucleation, and SWNT growth).

- (c) nucleation and growth
(d) termination.

In this contribution, we have developed a model that attempts to capture mathematically the kinetics of these stages.

A realistic kinetic model may be useful in the optimization of SWNT synthesis reactor design and operation. At the same time, it may serve as the basis for further understanding the growth mechanism. Therefore, we have attempted to minimize the number of empirical equations, using parameters with physical significance. To test the kinetic model and obtain typical values of the physical parameters, a series of experiments have been conducted on a CoMo/SiO₂ catalyst in a laboratory flow reactor at varying operating conditions. In this contribution, we present the model and its application to one specific case. Extension to other cases will be the subject of a later paper.

2. EXPERIMENTAL DETAILS

2.1. Catalyst Preparation and Characterization

A 2%wt CoMo/SiO₂ catalyst (1:3 Co/Mo molar ratio) was prepared by incipient wetness co-impregnation using an aqueous solution of (NH₄)₆Mo₇O₂₄·4H₂O and Co(NO₃)₂·6H₂O. The wet impregnated material was dried at 110 °C for 12 h and then calcined at 500 °C for 3 h in a convection oven.¹⁻⁹ XRD analysis of the catalyst during the various stages was conducted in a Bruker AXS Discovery G8, equipped with a GADDS detector. Raman spectroscopy was used to characterize the catalyst and the nanotube product. The Raman spectrometer used in this study is a Horiba Jobin-Yvon LabRam HR-800, equipped with a CCD detector and 1.96 eV (633 nm) laser.

The total carbon yield resulting from the SWNT synthesis reaction was determined by temperature programmed oxidation (TPO), as described in previous contributions.^{1,5,7}

2.2. Gas Evolution During SWNT Synthesis

As described elsewhere,¹⁻⁹ the SWNT synthesis reaction is typically performed in a vertical fluidized-bed quartz tube. The catalysts are pre-reduced in flowing H₂ up to 500 °C and the SWNT synthesis is conducted at 750 °C under pure CO for 30 min. In this work, to follow the kinetics of the SWNT synthesis, a mass spec (MKS 200 amu) was connected to the exit of the reactor by a stainless steel capillary (1/64" ID 1/16" OD) through an evacuated gas manifold kept at 0.5 Torr before entering the main chamber kept at 1.5×10^{-5} Torr. The mass range 1–50 amu was scanned every 6 seconds and a data point was recorded every 18 sec. All the masses (main ions and fragments) were followed to obtain quantitative data from the system. The correction for dispersion effects and residence time distributions is described in detail in Section 4.1.

2.3. Characterization of the SWNT Product

To confirm that the nanotubes produced during the kinetic measurements have the high quality that is characteristic of the CoMoCAT product, Raman spectroscopy (excitation laser 633 nm wavelength) was conducted on each sample investigated. As illustrated in Figure 2, the Raman

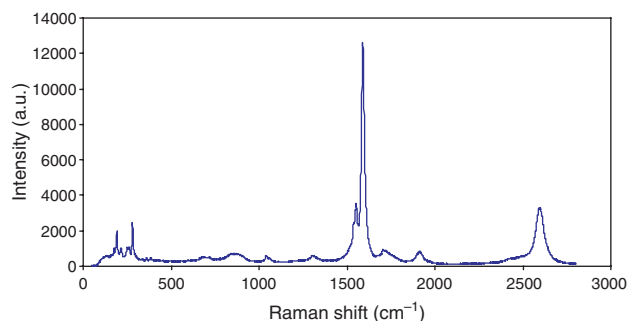


Fig. 2. Raman spectra of the SWNT product after 30 min in pure CO at 750 °C over 2% Co-Mo/SiO₂. Wavelength of excitation laser is 633 nm. Low values of D/G and D/D* are indicative of a low density of defects in the SWNT.

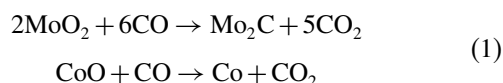
spectra obtained in each of the runs showed the typically strong G band with the G− and G+ clearly separated, without the metallic shoulder, a weak D band, and considerably strong RBM bands, corresponding to small diameter SWNT (most of them about 0.7–0.8 nm as characterized by optical absorption and photoluminescence).

3. STEPS CONSIDERED IN THE KINETIC MODEL OF THE SWNT SYNTHESIS

Specifically, the different stages considered in this mechanism for the kinetic model are the following:

3.1. Carburization of the Pre-Reduced Oxidic Phase and Generation of Active Sites

XRD analysis shows that in the calcined state the catalyst contains CoMoO_4 as the dominant species (see pattern b in Fig. 3(A)), in good agreement with Raman and UV-Vis studies previously reported by our group.^{3–5,7,8} After pre-reduction in H_2 , the XRD pattern indicates that the CoMoO_4 species is drastically altered (see pattern c in Fig. 3(A)). Contrary to the calcined sample, no crystalline CoMoO_4 phases are detected in the pre-reduced sample. Previous XPS and EXAFS results^{3–5,7,8} indicate that after pre-reduction in hydrogen and heating in He most of the Molybdenum is in a Mo(IV) state, which agrees with the appearance of MoO_2 in Figure 3(A), while all of the Cobalt remains as Co(II). After exposure to CO at 750 °C, an important transformation occurs during the first few minutes, the MoO_2 starts to disappear and in turn Mo_2C and metallic Co are clearly observed by XRD (see Fig. 3(B)). These data are in good agreement with previous EXAFS and Raman characterization data,^{3–5,7,8} that reveal that the formation of the carbide occurs during the first few minutes of exposure to CO. This reaction is most probably autocatalytic, leading to the formation of Mo_2C and metallic Co that can dissociate CO more readily than the oxidic species. Clearly, during this transformation, there is a significant amount of carbon uptake, with the concomitant evolution of CO_2 . Therefore, the kinetic model must take this carbon uptake into consideration. It is therefore essential to include carburization in the analysis since it is the process that creates the active sites and it also generates significant amount of CO_2 associated with the reduction of the oxidic phases. We can assume that the carburization step involves the following stoichiometric reactions:



As mentioned above, after the pre-reduction step, the oxidic species are in the form of Mo(IV) and Co(II), not necessarily as MoO_2 and CoO , but probably as a combination of bimetallic and monometallic oxides. Therefore, while the two stoichiometric reactions in (1) may

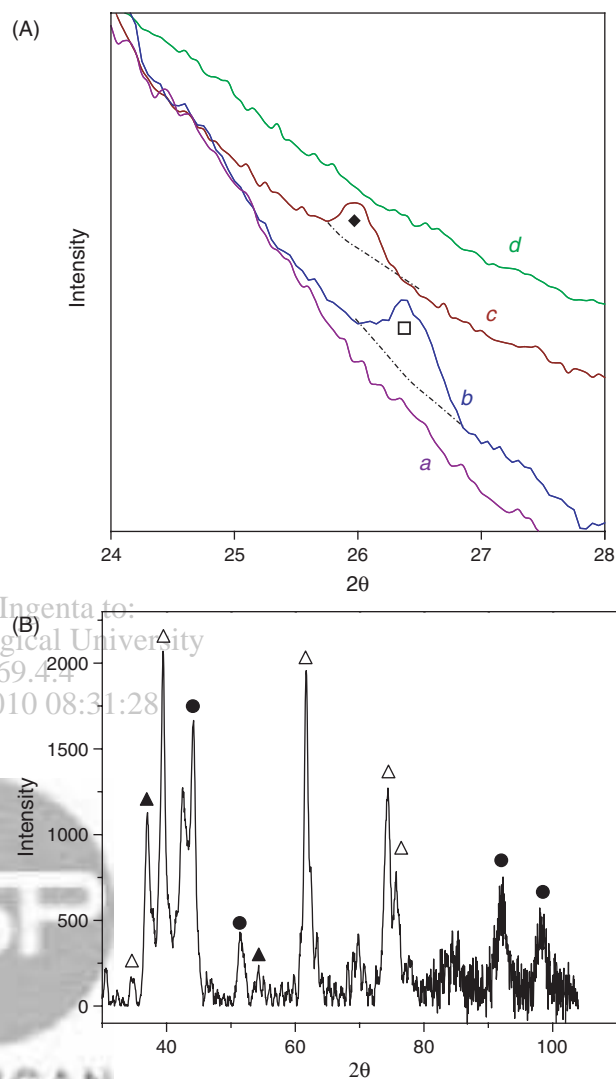


Fig. 3. (A) XRD patterns 24–28 range (a) SiO_2 support; (b) CoMo/ SiO_2 catalyst calcined at 500 °C; (c) reduced at 500 °C; (d) after 3 min reaction in CO at 750 °C. The open square symbol represents one of the expected diffraction peaks for CoMoO_4 , the full diamond corresponds to MoO_2 . (B) XRD of the nanotube product after removing the silica support by HF acid leaching and leaving the residual Co and Mo species on the nanotube product. The open triangle symbols represent the expected diffraction peaks for Mo carbide; the full triangles correspond to MoO_3 and the full circles correspond to metallic Co.

not reflect all the phases present in the catalyst, they are stoichiometrically valid and can be used to quantify the evolution of CO_2 . In fact, as shown below, the amount of CO_2 evolved during the carburization as estimated from the model is a good independent measure that, together with the independently measured total carbon yield, can be used to test the quantitative accuracy of the fit.

The carburization reaction is responsible for the creation of the active sites in the SWNT synthesis process. It involves the transformation of the CoMoO_x precursor into the active species (i.e., reduced Co clusters), as shown in Figure 1.

3.2. CO Dissociation Over the Surface of the Reduced Co Cluster

After the active sites have been generated, CO dissociates over the Co surface and carbon begins to accumulate increasing its surface concentration. While in the text, we refer to carbon concentration. The most correct term should be “surface fugacity” because the thermodynamic activity of these carbon species is not simply the concentration in equilibrium with the gas phase CO, but rather is the result of the several phenomena that occur on the surface; they are (i) the CO decomposition that generates surface C, (ii) the C diffusion (both across the surface and into the metal particle), and (iii) the reverse Boudouard reaction

of C with gas phase CO_2 . The first one causes an increase in the carbon surface fugacity, the last two act as releasing paths for carbon and help keeping a fraction of the surface clean.

3.3. Nucleation and Growth of SWNT

Two interfaces will be considered in the kinetic model. Interface 1 is the gas/Cobalt interface created after the catalyst activation. Interface 2 is the Cobalt/SWNT interface created after the SWNT caps have nucleated (see scheme in Figs. 4(a and b)). It is assumed that the carbon atoms from the CO dissociation enter into or onto the Co phase particles through the clean surface of the Co (*interface 1*), and they leave the Co phase through *interface 2* when forming the SWNT. As illustrated in Figure 5, the transport from interface 1 to interface 2 occurs by diffusion (surface or bulk) and is driven by the difference in chemical potential between the two interfaces. After the carbon concentration has reached a certain threshold, nucleation of ordered forms of carbon occur (e.g., hexagons^{24,25}). The formation of these nuclei generates interface 2 and the carbon flux is maintained because the nanotube structure provides a thermodynamic sink for the carbon and as a result the carbon concentration at the interface 2 is kept low.

3.4. Growth Termination

Based on the concept of two interfaces, we can envision two forms of nanotube growth termination. The first type of termination would occur at interface 1 by deactivation of the catalyst active sites, which result in a decrease of the fugacity C_S . The second type would occur at interface 2 when the carbon concentration, C_F , raises and

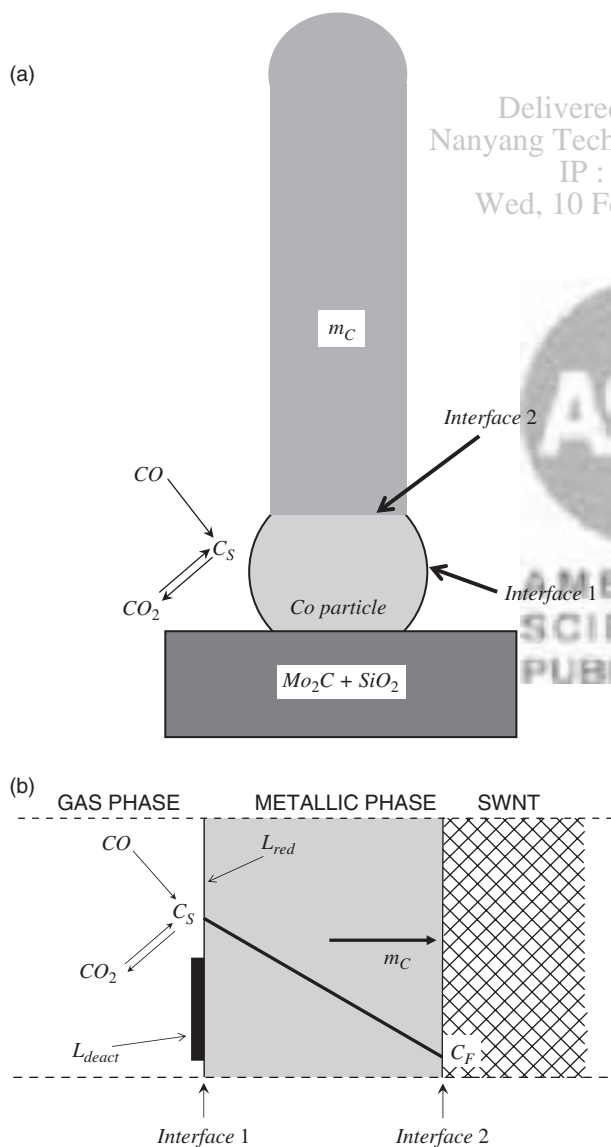


Fig. 4. (a) Scheme of the SWNT/catalyst system during synthesis depicting the two proposed interfaces, (1) metal/gas phase and (2) SWNT/metal. (b) Simplification of the two-interface system and interpretation of the diffusion of C atoms from interface 1 to interface 2.

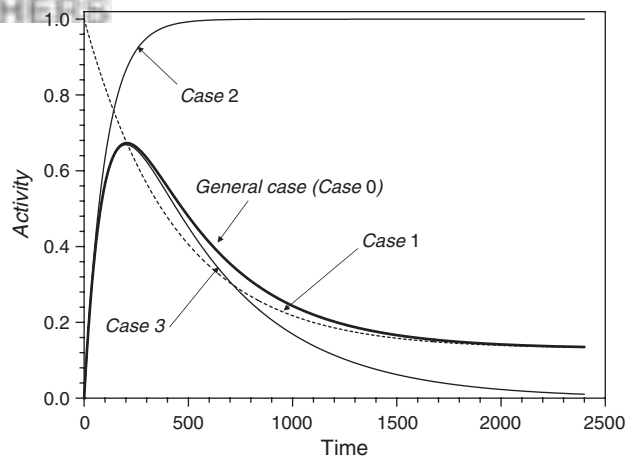


Fig. 5. Prediction of catalyst activity based on the different cases described in the text. Case 0: $\psi_a = 0.01$, $\psi_d = 0.002$, $\psi_r = 0.0003$ and $a_0 = 0$. Case 1: The initial activity is negligible ($a_0 = 0$) and the deactivation is irreversible ($\psi_r = 0$, $a_s = 0$). Case 2: $\psi_a = 0.01$, $\psi_d = 0$, $\psi_r = 0$ and $a_0 = 0$; and for Case 3: $\psi_a = 0$, $\psi_d = 0.002$, $\psi_r = 0.0003$ and $a_0 = 1$.

approaches C_S , thus eliminating the driving force for diffusion. As discussed below, the raising in C_F may be due to a mechanical interference of the nanotube growth with its environment, which would hinder the free path of C through the catalyst-nanotube interface 2.

4. MATHEMATICAL DESCRIPTION OF THE SWNT SYNTHESIS

4.1. Data Analysis

Due to the effect of residence time distribution, caused by the free volume in the reactor and lines connecting, the raw data obtained from the mass spec had to be deconvoluted to correlate the measured data with the real kinetics. Therefore, before using the data to fit the kinetic model a standard convolution–deconvolution method was employed. This method is the inverse problem of the response of a system to an inlet function. That is, at the exit of the free volume, we measure the response but need to obtain the concentration curve at the inlet of the free volume (i.e., the exit of the catalyst bed).

To obtain the residence time distribution of the free volume (reactor and connecting lines) a blank experiment was conducted using pure CO and an inert bed. The comparison of the output signal to an ideal step function allowed us to obtain the transfer function (E). Specifically, the derivative of the measured increase in CO in this blank experiment is the residence time distribution of the system. With this function, we used a standard data analysis method commonly used in reaction engineering.²⁶ According to this method, the concentration at the inlet of the free volume part, C_{in} , can be estimated as:

$$C_{in}(t') = F^{-1} \left[\frac{F[C_{out}(t)]}{F[E(t-t')]} \right]$$

where C_{out} is the measured outlet concentration at the end of the free volume part, $E(t-t')$ the experimentally obtained transfer function, and F and F^{-1} the *Fourier Transform* and the *Inverse Fourier Transform* respectively. These functions were obtained by a FFT numerical method. The resulting C_{in} is the desired CO₂ evolution that we can model to extract the kinetic parameters of the nanotube growth process.

4.2. Carburization and Activation

As mentioned above, during the initial carburization Mo(IV) becomes Mo₂C carbide and Co(II) becomes metallic Co. Furthermore, during carburization a large amount of CO₂ is produced due to the reduction process, resulting in 2.5 moles of CO₂ evolved per mole of Mo and 1 mole of CO₂ per mole of Co reacted.

To model the carburization process, we have used an equation initially proposed by Prout and Tompkins.^{27–29}

This equation can be expressed in terms of two parameters, k_c and K , and takes into account the autocatalytic effect of the metallic phase during the reduction/carburization step.

The rate of carburization is given by:

$$\frac{d\alpha}{dt} = k_c(1-\alpha)(1+K\alpha) \quad (2)$$

where α is the degree of carburization, defined as:

$$\alpha = \frac{L_{ox_0} - L_{ox}}{L_{ox_0}} = \frac{L_{car}}{L_{ox_0}} \quad (3)$$

The term $k_c(1-\alpha)$ in (2) represents the carburization of the fraction that is still oxidized while the term $(1+K\alpha)$ accounts for the autocatalytic character of the carburization.

The integration of Eq. (2) gives the evolution of the degree of carburization with time, which is needed for the activation of the catalyst, as follows:

$$\alpha = \frac{1 - \exp(-\psi_{carb} \cdot t)}{1 + K \cdot \exp(-\psi_{carb} \cdot t)} \quad (4)$$

where $\psi_{carb} = k_c \cdot (1 + K)$. The rate of CO₂ production during carburization step can be written as:

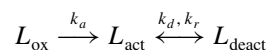
$$r_{carb} = \varepsilon_{carb} \cdot M_{CT} \cdot \frac{d\alpha}{dt} \quad (5)$$

where ε_{carb} is the carburization efficiency and varies from 0 to 1 ($\varepsilon_{carb} = 1$ implies total conversion of the oxide to carbide) and M_{CT} is the maximum stoichiometric amount of CO₂ generable by the catalyst. Substituting $\alpha(t)$ from Eq. (4) in Eq. (5) the rate of CO₂ production as a function of carburization time is obtained:

$$r_{carb} = \varepsilon_{carb} \cdot M_{CT} \cdot \frac{(1+K) \cdot \psi_{carb} \cdot \exp(-\psi_{carb} \cdot t)}{(1+K \exp(-\psi_{carb} \cdot t))^2} \quad (6)$$

The efficiency term is expected to be low under mild conditions and to increase under more severe conditions (e.g., higher pressure of CO and/or high temperature). In fact, the value for the product $\varepsilon_{carb} \cdot M_{CT}$ obtained from the fit can be directly compared to the experimental carbon content. The maximum carbon amount expected corresponds to the stoichiometry assumed in Eq. (1) and the metal loading of Co and Mo. This mass balance represents a testing of the quantitative validity of the model.

The evolution of all the sites of the catalyst can be summarized as:



The potential active sites (L_{ox}) become active sites (L_{act}) by carburization/reduction, and then can get deactivated during SWNT synthesis. L_{ox} is the molar concentration of potential sites (mol sites/g · cat) present on the catalyst, L_{act} is the concentration of reduced active sites (i.e., surface metallic Co sites), and L_{deact} is the concentration

of reduced but deactivated sites as a result of encapsulating carbon deposition. It is assumed that the reduction/carburization step is irreversible, but the deactivation is reversible. This reversibility is associated with the CO₂ gasification of carbon, i.e., the reverse Boudouard reaction.

While the carburization process determines the activation of the catalyst, the two phenomena are not identical. One is a bulk process, while the other involves the formation of a surface active site. Therefore, the values of the kinetic parameters that represent these two phenomena are related, but not the same. For the activation step, we assume that the transformation $L_{\text{ox}} \rightarrow L_{\text{act}}$ follows a first order kinetics:

$$-\frac{dL_{\text{ox}}}{dt} = \psi_a \cdot L_{\text{ox}} \quad (7)$$

where ψ_a is the “activation kinetic function” that depends on the operating conditions: $\psi_a = \varphi_a(T, p_T, p_{\text{CO}}, p_{\text{CO}_2})$. This function has been typically used in catalytic kinetic modeling when an induction period is involved.^{25, 30–34} In this case the CO conversion is low and it can be assumed that the reactor operates under differential conditions, therefore ψ_a is practically constant and the integration of Eq. (7) results in:

$$L_{\text{ox}} = L_{\text{ox}_0} \cdot \exp(-\psi_a \cdot t) \quad (8)$$

where L_{ox_0} represents the initial concentration of oxidized sites.

When carbon deposition starts, simultaneous deactivation of some of the sites by carbon encapsulation occurs. This is one of the two forms of growth termination considered in this model. Hence, the net rate of variation of active sites should be expressed as:

$$\frac{dL_{\text{act}}}{dt} = \psi_a \cdot L_{\text{ox}} - \psi_d \cdot L_{\text{act}} + \psi_r \cdot L_{\text{deact}} \quad (9)$$

where ψ_d and ψ_r are respectively the “deactivation and regeneration kinetic functions.” These kinetic functions also depend on the operating conditions: $\psi_d = \varphi_d(T, p_T, p_{\text{CO}}, p_{\text{CO}_2})$ and $\psi_r = \varphi_r(T, p_T, p_{\text{CO}}, p_{\text{CO}_2})$. In this case they have been assumed constant.

To solve Eq. (9), we can express the concentration of deactivated sites, L_{deact} , in terms of L_{ox} and L_{act} according the total site balance:

$$\begin{aligned} L_T &= L_{\text{ox}_0} + L_{\text{act}_0} \quad t = 0 \\ L_T &= L_{\text{ox}}(t) + L_{\text{act}}(t) + L_{\text{deact}}(t) \quad t = t \end{aligned} \quad (10)$$

We can use the dimensionless variables *catalyst activity*, a , and *potential catalyst activity*, a_p , as it is typically done in kinetic analysis in which there is change in the number of active site as a function of time of reaction (see for example Refs. [35–38]). The catalyst activity, a , is the fraction of active sites, and the potential catalyst activity, a_p , is the fraction of oxidized sites still available to be activated:

$$a = \frac{L_{\text{act}}}{L_T}; \quad a_p = \frac{L_{\text{ox}}}{L_T} \quad (11)$$

Now, the balance of active sites can be rewritten as:

$$a + a_p = 1 - \left(\frac{L_{\text{deact}}}{L_T} \right) \quad (12)$$

The rate of catalyst activation, Eq. (7) can now be expressed as:

$$-\frac{da_p}{dt} = \psi_a \cdot a_p \quad (13)$$

Integration of Eq. (13) yields:

$$a_p = (1 - a_0) \cdot \exp(-\psi_a \cdot t) \quad (14)$$

Likewise Eq. (9) becomes:

$$\begin{aligned} \frac{da}{dt} + (\psi_d + \psi_r) \cdot a \\ = \psi_r + (\psi_a - \psi_r) \cdot (1 - a_0) \cdot \exp(-\psi_a \cdot t) \end{aligned} \quad (15)$$

which with constant kinetic functions, ψ_a , ψ_d and ψ_r , can be integrated as:

$$a = a_s + \alpha_1 \cdot \exp(-\psi_a \cdot t) + \alpha_2 \cdot \exp(-\psi_G \cdot t) \quad (16)$$

where the terms ψ_G and a_s , α_1 and α_2 are lumped parameters given by:

$$\begin{aligned} \psi_G &= \psi_d + \psi_r; \quad a_s = \frac{\psi_r}{\psi_d + \psi_r} = \frac{\psi_r}{\psi_G} \\ \alpha_1 &= (1 - a_0) \cdot \left(\frac{\psi_a - \psi_r}{\psi_G - \psi_a} \right) \\ \alpha_2 &= (a_0 - a_s - \alpha_1) \end{aligned} \quad (17)$$

Equation (16) represents the time evolution of the catalyst activity, including an activation period and a reversible deactivation. As can be seen in Eq. (17), all the parameters involved can be expressed in terms of only three factors (ψ_a , ψ_d , and ψ_r) that have obvious physical significance.

This general expression can be simplified for specific cases, as follows:

Case 1. The initial activity is negligible ($a_0 = 0$) and the deactivation is irreversible ($\psi_r = 0$, $a_s = 0$). Under these conditions, Eq. (16) becomes:

$$a = \frac{\psi_a}{\psi_d - \psi_a} \exp(-\psi_a \cdot t) - \frac{\psi_a}{\psi_d - \psi_a} \exp(-\psi_d \cdot t) \quad (18)$$

Case 2. The initial activity is negligible ($a_0 = 0$) but the catalyst does not deactivate. Therefore $\psi_d = \psi_r = 0$ in Eq. (16), yielding:

$$a = 1 - (1 - a_0) \cdot \exp(-\psi_a \cdot t) \quad (19)$$

Case 3(a). The catalyst is initially activated ($a_0 = 1$), then, it does not require activation ($\psi_a = 0$). Deactivation is reversible, then the catalyst remains with residual activity, as illustrated in previous modeling studies.^{36–38}

$$a = a_s + (1 - a_s) \cdot \exp(-\psi_G \cdot t) \quad (20)$$

Case 3(b). The deactivation process is irreversible. Then $\psi_r = 0$, and:

$$a = \exp(-\psi_d \cdot t) \quad (21)$$

Figure 5 illustrates the time evolution of *catalyst activity* for the special cases described above. The values of the parameters used for the general case (case 0) were: $\psi_a = 0.01$, $\psi_d = 0.002$, $\psi_r = 0.0003$ and $a_0 = 0$. For case 1, the parameters were: $\psi_a = 0.01$, $\psi_d = 0.002$, $\psi_r = 0$ and $a_0 = 0$. For case 2, $\psi_a = 0.01$, $\psi_d = 0$, $\psi_r = 0$ and $a_0 = 0$; and for case 3 $\psi_a = 0$, $\psi_d = 0.002$, $\psi_r = 0.0003$ and $a_0 = 1$.

4.3. Rate of CO Dissociation and Carbon Deposition at Interface 1

After having developed an expression for the catalyst activity for the specific case, we can calculate the net rate of CO disproportionation on the surface using a typical rate expression for the Boudouard reaction:³⁹

$$(-r_{\text{CO}})_t = (-r_{\text{CO}})^0 \cdot a = k_1 \cdot \left(p_{\text{CO}} - \frac{p_{\text{CO}_2}}{K_{\text{eq}} p_{\text{CO}}} \right) \cdot a \quad (22)$$

where k_1 and K_{eq} are given by:

$$\begin{aligned} k_1 &= k_{1_0} \cdot \exp(-E_1/RT) \\ K_{\text{eq}} &= \frac{k_1}{k_2} = \exp(-\Delta G/RT) \end{aligned} \quad (23)$$

The term $(-r_{\text{CO}})^0$ represents the reaction rate of CO decomposition when the catalyst activity is 1, i.e., when is totally activated and before any deactivation process. Therefore, $(-r_{\text{CO}})^0$ is a constant value for a given operating conditions. In the case that the catalyst initially will be totally activated ($a_0 = 1$), this value is the initial reaction rate. Given the high reaction temperature at which the reaction is carried out, the terms of adsorption of CO and CO₂ can be neglected in the rate expression. From the effective rate of CO disproportionation, Eq. (22), and taking into account the stoichiometry of the reaction (2 CO: 1 C), the rate of carbon accumulated on the active metallic surface can be calculated as:

$$\frac{dC_S}{dt} = r_C = \frac{(-r_{\text{CO}})}{2} = \psi_S \cdot (C_{S_0} \cdot a - C_S) \quad (24)$$

In the above equation, the term ψ_S represent the “*intrinsic kinetic function of CO dissociation*” over the metallic surface (*interface 1*). We have considered that the rate of carbon deposition over the surface is proportional to the free surface and to the number of the available active sites to the reaction, i.e., the catalyst activity. Thus, the term C_{S_0} expresses the maximum surface concentration of carbon that can be formed over the fresh catalyst (i.e., without deactivation after total activation). This carbon concentration depends on the total active surface exposed by the

catalyst. Therefore, if the catalyst is deactivated by the formation of encapsulating coke and/or by sintering, the exposed metallic surface will be diminished. The evolution of C_S can be calculated solving the differential equation derived from the Eq. (24):

$$\frac{dC_S}{dt} + \psi_S \cdot C_S = \psi_S \cdot C_{S_0} \cdot a \quad (25)$$

In this equation, the evolution of the catalyst activity is given by the Eq. (19). The analytical solution of Eq. (25) is given by the following expression:

$$C_S = C_{S_0} \left[\begin{aligned} &a_S + \frac{\psi_S \cdot \alpha_1}{(\psi_S - \psi_a)} \exp(-\psi_a t) \\ &+ \frac{\psi_S \cdot \alpha_2}{(\psi_S - \psi_G)} \exp(-\psi_G t) \\ &- \alpha_3 \exp(-\psi_S t) \end{aligned} \right] \quad (26)$$

where the dimensionless term α_3 is given by:

$$\alpha_3 = a_S + \frac{\psi_S \cdot \alpha_1}{(\psi_S - \psi_a)} + \frac{\psi_S \cdot \alpha_2}{(\psi_S - \psi_G)} \quad (27)$$

4.4. Nucleation and Growth of SWNT at Interface 2

This stage represents the diffusion of carbon atoms through the metallic crystallites, i.e., from *interface 1* to *interface 2*, and in turn determines the rate of formation of SWNT. It must be noted that the mathematical representation of this phenomenon would be the same whether the diffusion occurs over the surface or through the bulk of the particle. In either case, the rate for this step can be expressed as:

$$r_{\text{SWNT}} = \frac{dm_C}{dt} = k_C (C_S - C_F) \quad (28)$$

The parameter k_C is the effective transport coefficient of carbon on or through the Co particles, and depends on the average size of the Co crystallites, d_{met} , the metallic exposed area, S_{met} , and of the carbon diffusivity of carbon on the metallic particle, $D_{C, \text{met}}$. In general, k_C can be approximated as:

$$k_C \approx (S_{\text{met}} \cdot \rho_{\text{met}}) \cdot (D_{C, \text{met}} / \bar{d}_{\text{met}}) \quad (29)$$

The carbon concentration at interface 2 is termed C_F , which has an initial value of zero and increases with time. However, when C_F reaches a value high enough to favor nucleation, formation of SWNT begins. As a result, a carbon sink is formed at this interface 2, and $C_F < C_S$.

If we consider $C_F \cong 0$, or also constant in time, we can directly solve Eq. (28) using Eq. (26) for the value of C_S :

$$r_{\text{SWNT}} = j_{C_0} \left[\begin{aligned} &a_S + \frac{\psi_S \cdot \alpha_1}{(\psi_S - \psi_a)} \exp(-\psi_a t) \\ &+ \frac{\psi_S \cdot \alpha_2}{(\psi_S - \psi_G)} \exp(-\psi_G t) \\ &- \alpha_3 \exp(-\psi_S t) \end{aligned} \right] \quad (30)$$

The term j_{C_0} represents the maximum allowable carbon flux ($g_C/g_{cat} \cdot s$) that can be obtained through the metallic particles of the catalysts, and is given by:

$$j_{C_0} = k_C \cdot C_{S_0} \quad (31)$$

Finally, we can calculate the total CO₂ evolution as the sum of the contribution from carburization and from SWNT growth:

$$r_{C_{tot}} = r_{C_{SWNT}} + r_{C_{carb}} \quad (32)$$

5. SIMULATIONS OF HYPOTHETICAL CASES WITH VARYING KINETIC PARAMETERS

The following simulations were conducted taking as a base case the following values for the kinetic parameters: $M_{CT}(\text{mol/g cat}) = 0.05$; $\psi_{carb}(\text{min}^{-1}) = 0.21$; $\psi_a(\text{min}^{-1}) = 0.015$; $\psi_d(\text{min}^{-1}) = 0.14$; $\psi_r(\text{min}^{-1}) = 0.009$; $\psi_s(\text{min}^{-1}) = 0.032$; $\xi_{FC}(\text{min}^{-1}) = 0.0035$; $(j_C)_0(\text{mol/g cat} \cdot \text{min}) = 0.045$.

5.1. Carburization Parameter (ψ_{carb})

As defined above, the carburization ψ_{carb} is a combination of the two kinetic constants k_C and $K_{autocat}$, which account for the carburization of the uncarburized fraction and the autocatalytic reaction, respectively. As shown in Figure 6, if the carburization parameter decreases with no changes in the other parameters, the position of the maximum carburization rate moves to longer times and the maximum value of carburization rate decreases. However, the area under the curve, which is given by M_{CT} remains

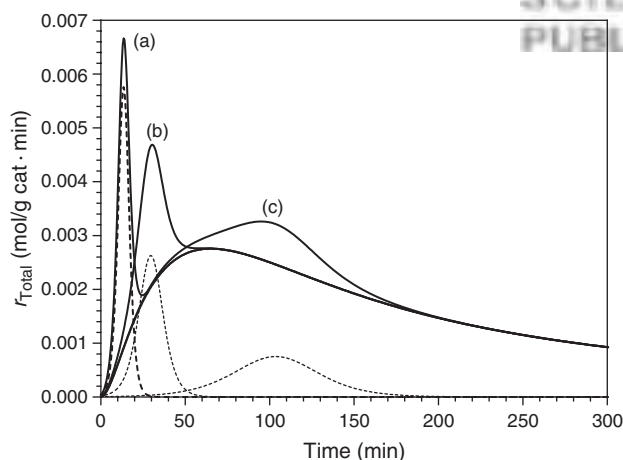


Fig. 6. Analysis of the effect of varying the carburization parameter ψ_{carb} while keeping the rest constant at the following values: $M_{CT}(\text{mol/g cat}) = 0.05$; $\psi_a(\text{min}^{-1}) = 0.015$; $\psi_d(\text{min}^{-1}) = 0.14$; $\psi_r(\text{min}^{-1}) = 0.009$; $\psi_s(\text{min}^{-1}) = 0.032$; $\xi_{FC}(\text{min}^{-1}) = 0.0035$; $(j_C)_0(\text{mol/g cat} \cdot \text{min}) = 0.045$. Curve (a) $\psi_{carb}(\text{min}^{-1}) = 0.46$; Curve (b) $\psi_{carb}(\text{min}^{-1}) = 0.21$; Curve (c) $\psi_{carb}(\text{min}^{-1}) = 0.06$.

unchanged. At the same time, if M_{CT} is decreased without changing ψ_{carb} the position of the peak does not change, but the maximum decreases.

5.2. Catalyst Activation Parameter (ψ_a)

The activation parameter ψ_a has an important effect on the overall shape of the curve. As shown in Figure 7, if ψ_a is increased while leaving the rest unchanged, a rapid increase in the rate of SWNT formation together with an increase in the total yield of SWNT are observed. Similar effects are observed if the *intrinsic kinetic function of CO dissociation*, ψ_s is increased, which reflects how difficult it is to decouple some of these kinetic parameters.

5.3. Catalyst Deactivation Parameter (ψ_d)

The deactivation parameter ψ_d has also an important effect on the overall shape of the curve. As shown in Figure 8, if ψ_d is increased while leaving the rest unchanged, a rapid decrease in the rate of SWNT formation, together with a decrease in the total yield of SWNT are observed. It is noteworthy that this decrease is observed just from the beginning of the reaction and therefore an increase of ψ_d has a parallel effect with a decrease in ψ_a , which increases the uncertainties of the model.

5.4. Termination by Steric Hindrance (ξ_{FC})

In addition to the termination by catalyst deactivation one can consider the possibility that, as carbon accumulates by increasing length and number of SWNT within the porous structure, physical hindrance for the free displacement of



Fig. 7. Analysis of the effect of varying the activation parameter ψ_a while keeping the rest constant at the following values: $M_{CT}(\text{mol/g cat}) = 0.05$; $\psi_{carb}(\text{min}^{-1}) = 0.21$; $\psi_d(\text{min}^{-1}) = 0.14$; $\psi_r(\text{min}^{-1}) = 0.009$; $\psi_s(\text{min}^{-1}) = 0.032$; $\xi_{FC}(\text{min}^{-1}) = 0.0035$; $(j_C)_0(\text{mol/g cat} \cdot \text{min}) = 0.045$. Curve (a) $\psi_a(\text{min}^{-1}) = 0.15$; Curve (b) $\psi_a(\text{min}^{-1}) = 0.015$; Curve (c) $\psi_a(\text{min}^{-1}) = 0.0015$.

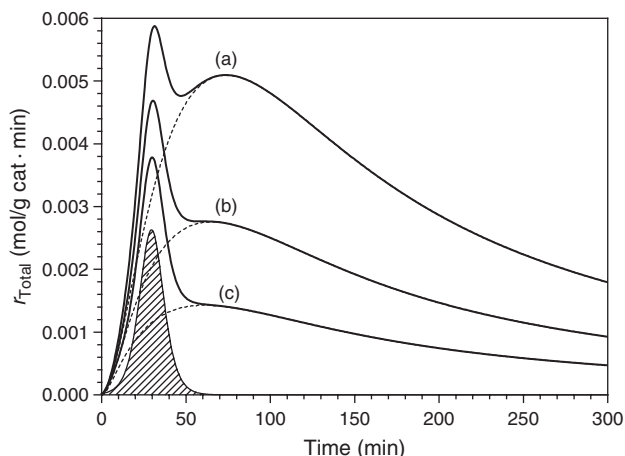


Fig. 8. Analysis of the effect of varying the deactivation parameter ψ_d while keeping the rest constant at the following values: M_{CT} (mol/g cat) = 0.05; ψ_{carb} (min^{-1}) = 0.21; ψ_a (min^{-1}) = 0.015; ψ_s (min^{-1}) = 0.009; ψ_g (min^{-1}) = 0.032; ξ_{FC} (min^{-1}) = 0.0035; $(j_C)_0$ (mol/g cat · min) = 0.045. Curve (a) ψ_d (min^{-1}) = 0.07; Curve (b) ψ_d (min^{-1}) = 0.14; Curve (c) ψ_d (min^{-1}) = 0.28.

the growing nanotubes may occur. This mechanical restriction of the growing nanotube may make the insertion of new carbon atoms at *interface 2* more difficult. One may speculate that the magnitude of this hindrance may be a function not only of the length and number of SWNT, but also of the nature of the surrounding environment at the growing site. That is, the interaction of a growing SWNT with the catalyst support and/or with other nanotubes may vary depending on the pore size of the catalyst, the metal content, etc. The larger is the volume of nanotubes compared to the available space the more restricted will be the insertion of new carbon atoms at the interface.

In fact, there have been several examples in which individual SWNT has been allowed to grow practically free of interaction with the catalyst surface or other nanotubes. For example, Liu et al.^{40,41} have grown SWNT in the 1–2 cm range when the catalyst was deposited on an edge by photolithography and the growing SWNT was suspended in the flowing gas, thus avoiding hindering its growth by interaction with neither other nanotubes nor the substrate surface. The authors called this phenomenon “kite-mechanism” to illustrate the growth of a long nanotube tail, aligned in the direction of the flow. Other examples of long SWNT have been observed when the substrate is flat and the growing end is open.^{42,43} By contrast, when the growth is conducted on a typical high-surface-area porous catalyst, the growth process is eventually impeded by the lack of space for displacement inside the pores and tube–tube interactions. Therefore, in addition to catalyst deactivation, a second type of growth termination that should be considered in the model is the steric hindrance.

To take into account these considerations, we assume that the value of C_F is proportional to the amount of carbon accumulated with a proportionality constant ξ_F that

depends on the structure of the catalyst substrate and how the growing SWNT accommodate in such structure. Therefore,

$$C_F = \xi_F \cdot m_C \quad (33)$$

Accordingly, for an open structure, with very low hindrance for the growth of the SWNT, ξ_F should be low. By contrast, for a constricted catalyst structure (e.g., low pore volume), ξ_F should take higher values.

This is an interesting result and presents an alternative possibility to explain the typically observed SWNT growth termination, which is commonly ascribed to catalyst deactivation only.⁴⁴ More recently Iijima et al.⁴⁵ have indicated that they have obtained maximum catalyst utilization when the catalyst particles are sparse, a concept which is in line with our quantifiable hindrance factor (ξ_{FC}). The influence of this factor is clearly envisioned when the growth occurs inside a catalyst pore, but it may also be applicable in the case of nanotube forest growth on flat surfaces. As we have previously shown,⁴⁶ the nanotubes in the forest grow connected to each other by a crust that forms on the top. The mechanical constriction that this crust imposes to the growing nanotubes may also be described in terms of a hindrance factor.

From Eq. (28), the variation of the rate of carbon production can now be expressed as:

$$\frac{dm_C}{dt} + \xi_{FC} m_C = k_C C_S \quad (34)$$

where the term ξ_{FC} is given by:

$$\xi_{FC} = \xi_F \cdot k_C \quad (35)$$

After substitution of Eq. (26) into Eq. (34), can be obtained the analytical solution of this equation:

$$m_C = j_{C_0} \left[\begin{array}{l} A_0 + A_1 \exp(-\psi_a t) + A_2 \exp(-\psi_G t) \\ - A_3 \exp(-\psi_S t) - A_4 \exp(-\xi_{FC} t) \end{array} \right] \quad (36)$$

The constants appearing in the above equation are given by the following expressions:

$$\begin{aligned} A_0 &= \frac{a_S}{\xi_{FC}}, & A_1 &= \frac{\alpha_1 \cdot \psi_S}{(\psi_S - \psi_a)(\xi_{FC} - \psi_a)} \\ A_2 &= \frac{\alpha_2 \cdot \psi_S}{(\psi_S - \psi_G)(\xi_{FC} - \psi_G)} \\ A_3 &= \frac{\alpha_3}{(\xi_{FC} - \psi_S)}, & A_4 &= A_0 + A_1 + A_2 - A_3 \end{aligned} \quad (37)$$

The rate of SWNT production is directly obtained from the derivative of the Eq. (37):

$$\begin{aligned} r_{C_{SWNT}} &= \frac{dm_C}{dt} = \\ &= j_{C_0} \left[\begin{array}{l} -\psi_a A_1 \exp(-\psi_a t) \\ -\psi_G A_2 \exp(-\psi_G t) \\ +\psi_S A_3 \exp(-\psi_S t) \\ +\xi_{FC} A_4 \exp(-\xi_{FC} t) \end{array} \right] \quad (38) \end{aligned}$$

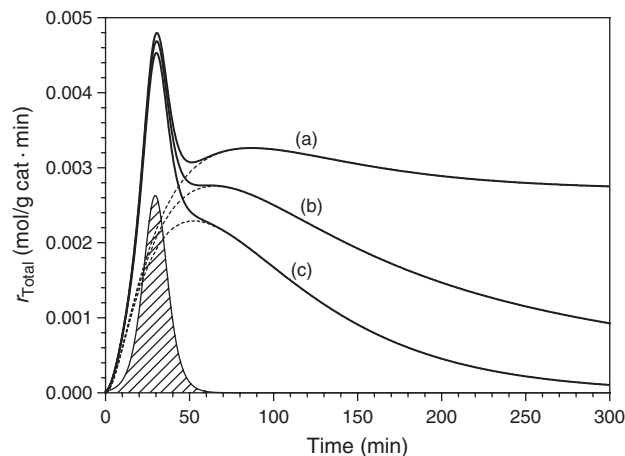


Fig. 9. Analysis of the effect of varying the hindrance factor ξ_{FC} while keeping the rest constant at the following values: $M_{CT}(\text{mol/g cat}) = 0.05$; $\psi_{\text{carb}}(\text{min}^{-1}) = 0.21$; $\psi_a(\text{min}^{-1}) = 0.015$; $\psi_r(\text{min}^{-1}) = 0.009$; $\psi_s(\text{min}^{-1}) = 0.032$; $(j_C)_0(\text{mol/g cat} \cdot \text{min}) = 0.045$; $\psi_d(\text{min}^{-1}) = 0.14$. Curve (a) $\xi_{FC}(\text{min}^{-1}) = 0.0001$; Curve (b) $\xi_{FC}(\text{min}^{-1}) = 0.0035$; Curve (c) $\xi_{FC}(\text{min}^{-1}) = 0.0090$.

Again, Eq. (32) gives the total rate of CO_2 evolution observed at the exit of the reactor, but now the rate due to SWNT growth is given by Eq. (38) that corresponds to a case more general than Eq. (30).

An example of simulations in which only the hindrance factor has been varied is shown in Figure 9. It is clear that as ξ_{FC} increases the rate of SWNT production decreases causing similar effect as the catalyst deactivation. In fact, for high values of ξ_{FC} the growth rate becomes practically zero. An interesting difference with catalyst deactivation is seen when comparing Figures 8 and 9. While an increase in catalyst deactivation causes a decrease in rate from the very beginning, the effect of the hindrance factor is only apparent after a certain amount of carbon has been deposited.

6. APPLICATION OF THE MODEL TO AN EXPERIMENTAL CASE

Several experiments have been conducted under different operating conditions, monitoring the evolution of CO_2 during the reaction in order to determine the influence of the

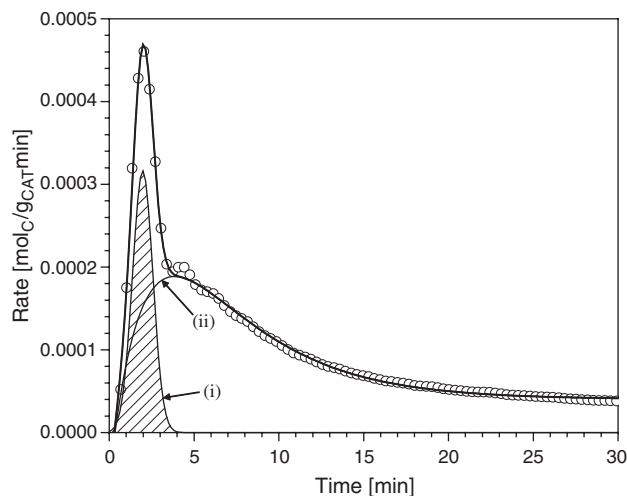


Fig. 10. Typical experimental rate profile of CO_2 evolution as a function of time (symbols) plotted together with the fitting obtained with the kinetic model. Two regions are clearly differentiated: (i) a sharp evolution of CO_2 in the first minutes associated with the carburization of the oxidic phase and (ii) an activation–deactivation profile that is associated with the nanotube growth. The kinetic parameters resulting from this fit are reported in Table I.

reaction temperature, feed composition and total pressure over the kinetics of SWNT growth. In the present paper we apply the new kinetic model to a specific case after deconvolution of the mass spec signal as explained in the experimental section. In a subsequent paper we will report the application of the model under varying experimental conditions.

In Figure 10 a typical rate profile as a function of time is presented together with the fitting obtained with the kinetic model. The two regions described in the previous simulations are clearly differentiated in the experimental case: (i) a sharp evolution of CO_2 in the first minutes, that is associated with the carburization of the oxidic phase ($r_{C_{\text{carb}}}$), and (ii) an activation–deactivation profile that is associated with the growth of SWNT (r_{CSWNT}). These facts are consistent with the simulations presented above.

The kinetic parameters are reported in Table I, together with the errors for 95% confidence. The quality of the fit is excellent, indicating that the model captures well the experimental behaviour of the catalyst under reaction

Table I. Results of kinetic model fitting of a typical run. Reaction temperature: 700 °C, P_{CO} : 20 psig.

Carburization			SWNT production			Mass balance	
Parameters	Value	Stand. error	Parameters	Value	Stand. error	Carburization	
M_{CT}	$5.33 \cdot 10^{-4}$	$\pm 7.63 \cdot 10^{-5}$	ψ_a	0.765	± 30.6	Fit	Measured
K	151	± 56.4	ψ_d	0.181	± 0.202	0.53 mmol	0.49 mmol
ε	1.00	± 0	ψ_r	0.086	± 0.070	SWNT production	
ψ_C	2.58	± 0.177	ψ_s	0.0290	± 0.0208	Fit	Measured
			r_{C_0}	0.0093	± 0.375	3.01 mmol	3.05 mmol
			ξ_{FC}	0.788	± 31.8		

$$\chi^2/DoF = 5.8244 \cdot 10^{-11}$$

$$R^2 = 0.99328.$$

conditions, and provides quantifiable values of the physical parameters.

For example, as seen in Table I the closure of the carbon balance during carburization and reaction gives validity to the fitting. For the carburization step, the fitted values of the shaded area (0.53 mmol) compare very well with the amount resulting from the stoichiometric reactions (0.49 mmol) described before, Eq. (1). The remaining area—under the bold line—(3.01 mmol) can be compared with the experimental data obtained by TPO (3.05 mmol), so the effective amount of SWNT present on the sample.

7. SUMMARY

A multi-step kinetic model has been developed to describe the SWNT synthesis by CO disproportionation on a CoMo/SiO₂ catalyst (CoMoCAT). The model takes into consideration all the relevant steps in the process of SWNT growth:

- catalyst carburization and catalyst activation
- CO decomposition over active sites
- nucleation of ordered forms of carbon and nanotube growth
- termination by catalyst deactivation or steric hindrance.

The application of the kinetic model to the experimental data allows separating the carburization step and the growth of SWNT. In order to have realistic values of the experimental data a deconvolution procedure must be done to the raw data to avoid any experimental artifact that could disguise the real values of the kinetic parameters.

A novel aspect of this model is the consideration of two possible forms of growth termination. One of them is the deactivation of active sites and the other the carbon saturation at the metal-nanotube interface. The role of the catalyst pore structure and nanotube–nanotube interaction in this termination has been contemplated with the definition of a novel hindrance factor that takes into account the effect of the amount of carbon deposited on the surface on the growth rate.

Acknowledgments: The authors gratefully acknowledge the financial support from Department of Energy (Grant DE-FG03-02ER15345). A. Monzon also acknowledges financial support to Regional Government of Aragón, Spain (DGA, Departamento de Ciencia Tecnología y Universidad) and University of Zaragoza.

References and Notes

1. B. Kitiyanan, W. E. Alvarez, J. H. Harwell, and D. E. Resasco, *Chem. Phys. Lett.* 317, 497 (2000).
2. D. E. Resasco, W. E. Alvarez, F. Pompeo, L. Balzano, J. E. Herrera, B. Kitiyanan, and A. Borgna, *J. Nanopart. Res.* 4, 131 (2002).
3. D. E. Resasco, J. E. Herrera, and L. Balzano, *J. Nanosci. Nanotechnol.* 4, 398 (2004).
4. D. E. Resasco, J. E. Herrera, and L. Balzano, *J. Nanosci. Nanotechnol.* 3, 1 (2003).
5. J. E. Herrera, L. Balzano, A. Borgna, W. E. Alvarez, and D. E. Resasco, *J. Catal.* 204, 129 (2001).
6. L. Zhang, L. Balzano, and D. E. Resasco, *J. Phys. Chem. B* 109, 14375 (2005).
7. W. E. Alvarez, B. Kitiyanan, A. Borgna, and D. E. Resasco, *Carbon* 39, 547 (2001).
8. J. E. Herrera and D. E. Resasco, *J. Catal.* 221, 354 (2004).
9. G. Lolli, L. A. Zhang, L. Balzano, N. Sakulchaicharoen, Y. Q. Tan, and D. E. Resasco, *J. Phys. Chem. B* 110, 2108 (2006).
10. S. M. Bachilo, L. Balzano, J. E. Herrera, F. Pompeo, D. E. Resasco, and R. B. Weisman, *J. Am. Chem. Soc.* 125, 11186 (2003).
11. Z. Zhu, J. Crochet, M. S. Arnold, M. C. Hersam, H. Ulbricht, D. Resasco, and T. Hertel, *J. Phys. Chem. C* 111, 3831 (2007).
12. A. Jorio, A. P. Santos, H. B. Ribeiro, C. Fantini, M. Souza, J. P. M. Vieira, C. A. Furtado, J. Jiang, R. Saito, L. Balzano, D. E. Resasco, and M. A. Pimenta, *Phys. Rev. B* 72, Art. No. 075207 (2005).
13. S. G. Chou, H. B. Ribeiro, E. B. Barros, A. P. Santos, D. Nezhich, G. G. Samsonidze, C. Fantini, M. A. Pimenta, A. Jorio, F. Plentz Filho, M. S. Dresselhaus, G. Dresselhaus, R. Saito, M. Zheng, G. B. Onoa, E. D. Semke, A. K. Swan, M. S. Unlu, and B. B. Goldberg, *Chem. Phys. Lett.* 397, 296 (2004).
14. Y. Maeda, M. Kanda, M. Hashimoto, T. Hasegawa, S. Kimura, Y. F. Lian, T. Wakahara, T. Akasaka, S. Kazaoui, N. Minami, T. Okazaki, Y. Hayamizu, K. Hata, J. Lu, and S. Nagase, *J. Am. Chem. Soc.* 128, 12239 (2006).
15. M. Zheng and E. D. Semke, *J. Am. Chem. Soc.* 129, 6084 (2007).
16. Y. Maeda, M. Kanda, M. Hashimoto, T. Hasegawa, S. Kimura, Y. Lian, T. Wakahara, T. Akasaka, S. Kazaoui, N. Minami, T. Okazaki, Y. Hayamizu, K. Hata, J. Lu, and S. Nagase, *J. Am. Chem. Soc.* 128, 12239 (2006).
17. N. Nair, M. L. Usrey, W. J. Kim, R. D. Braatz, and M. S. Strano, *Anal. Chem.* 78, 7689 (2006).
18. N. Nair, M. L. Usrey, W. J. Kim, R. D. Braatz, and M. S. Strano, *Anal. Chem.* 78, 7689 (2006).
19. P. B. Balbuena, J. Zhao, S. P. Huang, Y. X. Wang, N. Sakulchaicharoen, and D. E. Resasco, *J. Nanosci. Nanotechnol.* 6, 1247 (2006).
20. E. Lamouroux, P. Serp, and P. Kalck, *Catal. Rev.* 49, 341 (2007).
21. J. Zhao and P. B. Balbuena, *J. Phys. Chem. A* 110, 2771 (2006).
22. F. Ding, A. Rosén, and K. Bolton, *AIP Conf. Proc.* 723, 364 (2004).
23. F. Ding, A. Rosén, and K. Bolton, *Comp. Mater. Sci.* 35, 243 (2006).
24. J. Zhao, A. Martinez-Limia, and P. B. Balbuena, *Nanotechnology* 16, S575 (2005).
25. K. Bolton, F. Ding, and A. J. Rosen, *J. Nanosci. Nanotechnol.* 6, 1211 (2006).
26. T. Lilledahl, K. Sjöström, and L. P. Wiktorsson, *AIChE J.* 37, 1415 (1991).
27. E. G. Prout and F. C. Tompkins, *Trans. Faraday Soc.* 40, 488 (1944).
28. B. Delmon, *Bull. Soc. Chim. France* 590 (1961).
29. T. V. Hiep and S. Kaliaguine, *Chem. Eng. Sci.* 28, 195 (1973).
30. J. I. Villacampa, C. Royo, E. Romeo, J. A. Montoya, P. Del Angel, and A. Monzón, *Appl. Catal. A: Gen.* 252, 363 (2003).
31. M. Pérez-Cabero, E. Romeo, C. Royo, A. Monzón, A. Guerrero-Ruiz, and I. Rodríguez-Ramos, *J. Catal.* 224, 197 (2004).
32. D. Farcasiu, J. O. Li, and A. Kogelbauer, *J. Molec. Catal. A* 124, 67 (1997).
33. E. L. Agorreta, J. A. Peña, J. Santamaria, and A. Monzón, *Ind. Eng. Chem. Res.* 30, 111 (1991).
34. P. Mcallister and E. E. Wolf, *J. Catal.* 138, 129 (1992).
35. M. Morbidelli, A. Servida, and A. Varma, *Ind. Eng. Chem. Fund.* 21, 278 (1982).
36. A. L. Pozzi and H. F. Rase, *Ind. Eng. Chem.* 50, 1075 (1958).

37. J. Corella, J. Adanez, and A. Monzón, *Ind. Eng. Chem. Res.* 27, 375 (1988).
38. A. Borgna, T. F. Garetto, A. Monzón, and C. R. Apesteguía, *J. Catal.* 146, 69 (1994).
39. J. W. Snoeck, G. F. Froment, and M. Fowles, *Ind. & Eng. Chem. Res.* 41, 4252 (2002).
40. S. Huang, M. Woodson, R. Smalley, and J. Liu, *Nano Lett.* 4, 1025 (2004).
41. L. X. Zheng, M. J. O'Connell, S. K. Doorn, X. Z. Liao, Y. H. Zhao, E. A. Akhadvov, M. A. Hoffbauer, B. J. Roop, Q. X. Jial, R. C. Dye, D. E. Peterson, S. M. Huang, J. Liu, and Y. T. Zhu, *Nat. Mater.* 3, 673 (2004).
42. K. Hata, D. N. Futaba, K. Mizuno, T. Namai, M. Yumura, and S. Iijima, *Science* 306, 1362 (2004).
43. L. Zhang, Y. Tan, and D. E. Resasco, *Chem. Phys. Lett.* 422, 198 (2006).
44. D. N. Futaba, K. Hata, T. Yamada, K. Mizuno, M. Yumura, and S. Iijima, *Phys. Rev. Lett.* 95, 056104 (2005).
45. D. N. Futaba, K. Hata, T. Namai, T. Yamada, K. Mizuno, Y. Hayamizu, M. Yumura, and S. Iijima, *J. Phys. Chem. B* 110, 8035 (2006).
46. L. Zhang, Z. Li, Y. Tan, G. Lolli, N. Sakulchaicharoen, F. G. Requejo, B. S. Mun, and D. E. Resasco, *Chem. Mat.* 18, 5624 (2006).

Received: 15 May 2007. Revised/Accepted: 24 October 2007.

Delivered by Ingenta to:
Nanyang Technological University
IP : 155.69.4.4
Wed, 10 Feb 2010 08:31:28

